RESEARCH ARTICLE

ADVANCED
ENERGY & SUSTAINABILITY
RESEARCH
Open Access

www.advenergysustres.com

Effect of Sintering Temperature on the Thermoelectric Properties of Ag$_2$Se Fabricated by Spark Plasma Sintering with High Compression

Dulyawich Palaporn, Ken Kurosaki,* and Supree Pinitsoontorn*

Silver selenide (Ag$_2$Se) is a high-performance thermoelectric (TE) material near room temperature. This research improves its TE figure-of-merit (ZT) by varying the sintering temperatures (423–723 K) in the spark plasma sintering (SPS) process with high compression pressure (300 MPa). The SPS compaction of Ag$_2$Se powders synthesized by wet chemical reaction leads to the fast fusion of particles so that the grain boundaries are hardly visible. Furthermore, the fast fusion causes nanopores at the grain surface and some cracks, particularly at higher sintering temperatures. These featured microstructures decrease carrier concentrations and affect the TE properties significantly. The TE measurements show that increasing sintering temperatures results in decreased electrical conductivity and increased magnitude of the Seebeck coefficient due to microstructural defects. Increasing SPS temperatures also suppresses the thermal conductivity from enhancing phonon scattering by defects. The bulk Ag$_2$Se sample sintered at 723 K shows the best TE performance with the maximum ZT of 0.90 with a slight variation from 300 to 400 K. Thus, the high-temperature SPS with high-compression pressure is likely to be the key for fabricating bulk Ag$_2$Se with high TE performance.

1. Introduction

Thermoelectric (TE) materials are well known for their uses in an electrical generator, the so-called radioisotope thermoelectric generator (RTG), in space explorer missions. The Mars mission rovers, Curiosity and Perseverance, use RTG instead of solar power due to low-intensity sunlight in the long Mars winter and thick Marian dust which can quickly cover solar cells.[1–4] Conversely, RGT can directly convert heat from a radiation source to electricity without moving parts and causes no noise.[5]

The performance of the RGT relies on the efficiency of TE materials, defined by the dimensionless figure-of-merit (ZT)

$$ZT = S^2\sigma T/\kappa \tag{1}$$

where S, σ, κ, and T are the Seebeck coefficient, electrical conductivity, thermal conductivity, and absolute temperature, respectively.[6] The higher the ZT, the better the heat-to-electricity conversion efficiency of TE materials and RGT.

The performance of a TE material depends on the operating temperature. For example, silicon and lead telluride have operating temperatures of around 1000–1200 K,[7,8] and 600–1000 K,[9–11] respectively. However, very few high-performance TE materials at room temperature have been reported. So far, the best TE material at room temperature belongs to the bismuth telluride (Bi$_2$Te$_3$) and related alloys with their ZT around 1.0.[12] Nonetheless, its constituents, i.e., Bi and Te, are very rare and could be toxic.[13] Thus, new candidate TE materials at room temperature or near room temperature should be investigated.

Silver selenide (Ag$_2$Se) is another TE material that has an operating temperature near room temperature with ZT close to 1.0.[14–16] Its constituents are also more earth-abundant and less toxic compared to Bi$_2$Te$_3$. Ag$_2$Se in an orthorhombic phase (β-Ag$_2$Se) at a temperature below 407 K is a narrow bandgap semiconductor with good TE properties.[17,18] Above 407 K, β-Ag$_2$Se transforms into a metallic phase with a cubic structure

D. Palaporn, S. Pinitsoontorn
Department of Physics
Faculty of Science
Khon Kaen University
Khon Kaen 40002, Thailand
E-mail: psupree@kku.ac.th

The ORCID identification number(s) for the author(s) of this article can be found under https://doi.org/10.1002/aesr.202300082.

K. Kurosaki
Institute for Integrated Radiation and Nuclear Science
Kyoto University
2, Asashiro-Nishi, Kumatori-cho, Sennan-gun, Osaka 590-0494, Japan
E-mail: kurosaki.ken.6n@kyoto-u.ac.jp

K. Kurosaki
Research Institute of Nuclear Engineering
University of Fukui
1-3-33 Kanawa-cho, Tsuruga, Fukui 914-0055, Japan

S. Pinitsoontorn
Institute of Nanomaterials Research and Innovation for Energy (IN-RIE)
Khon Kaen University
Khon Kaen 40002, Thailand

(α-Ag$_2$Se). Dynamic self-doping of Ag atoms occurs in the matrix, which leads to undesired TE properties.[19–21]

There has been much effort to enhance the ZT of Ag$_2$Se using numerous strategies. Manipulation of carrier concentration is among the best strategy to increase the ZT of Ag$_2$Se. For example, Jood et al. doped excess selenium and sulfur to reduce dynamic Ag self-doping. The carrier concentration was decreased from 6×10^{18} to $3.5 \times 10^{18}\,cm^{-3}$, contributing to an increased ZT of 0.9 throughout the observed temperature range.[19] In contrast, substituting Cu for Ag caused an increase in the carrier concentration from 3.5×10^{18} to $4.5 \times 10^{18}\,cm^{-3}$, which consequently suppressed ZT to 0.7 at 300 K.[20] Theoretically, Chen et al. calculated that a maximum ZT of 1.2 can be reached by decreasing the carrier concentration to approximately $1.0 \times 10^{18}\,cm^{-3}$. They also showed that a hierarchical Ag$_2$Se structure could be formed by increasing the sintering temperature, contributing to the decreased carrier concentration of $3.5 \times 10^{18}\,cm^{-3}$ and, hence, the ZT of 0.9 at 400 K.[15] Therefore, decreasing Ag$_2$Se carrier concentration is crucial to enhance the ZT of Ag$_2$Se.

Spark plasma sintering (SPS) is a common method used to prepare bulk TE samples. The sintering temperature and compression pressure should be optimized for each material. However, very few research has investigated the effect of SPS conditions on the consolidation of Ag$_2$Se powders. For instance, Chen et al. studied the effect of SPS temperature of Ag$_2$Se powders prepared by solid-state ball milling.[15] However, the dependence of sintering temperature on the TE properties of Ag$_2$Se was hardly observed when the SPS temperature was higher than 373 K. Also, the compression pressure was limited to ≈100 MPa due to the attainable pressure by using a graphite die. Thus, in this work, the effect of sintering temperatures on the TE properties of bulk Ag$_2$Se was studied. Moreover, a hardened steel die with a compressive strength of up to 350 MPa was used instead

of a graphite die. Using a higher compression pressure would help in forming fully dense bulk samples. Our research goal is to elucidate the mechanism and influence of sintering temperature with high compression on the microstructure and TE properties of the Ag$_2$Se bulk material. In addition, the Ag$_2$Se powders before SPS were synthesized via a wet chemical reaction. This synthesis process can reduce the Ag$_2$Se particle size lower than synthesis by ball milling. The smaller sizes would lead to smaller grains, which can aid in enhancing TE properties.

2. Results and Discussion

The phase and crystallinity of bulk Ag$_2$Se samples after SPS were observed using X-ray diffraction (XRD), as shown in **Figure 1**. The XRD pattern indicates the orthorhombic phase (β-Ag$_2$Se) for all samples with the two main peaks at 2θ of 33.5° and 34.7° representing the (112) and (121) reflective planes. The magnified view for the 2θ position of the (112) and (121) planes is shown on the right of Figure 1. The peak positions of all samples and the reference are nearly the same, implying similar lattice parameters. The patterns were fitted using Rietveld refinement. The observations, calculations, and differences are represented by the black, red, and blue lines in Figure 1, while the goodness of fit (χ^2), R_p, and R_{wp} are also displayed in this figure. Furthermore, the lattice parameters and unit cell volume were calculated, as presented in **Table 1**. The lattice parameters fluctuate slightly with the SPS temperatures, but the variation is less than 0.3%. The lattice parameters of all samples are also close to those of the reference. In addition, Table 1 shows the crystallite sizes, determined using the Scherrer formula,[22] which increase monotonically with the sintering temperature from 287 ± 8 nm at 423 K to 367 ± 8 nm at 723 K.

The morphology of the bulk samples at different SPS temperatures is observed from the SEM images, as shown in **Figure 2**.
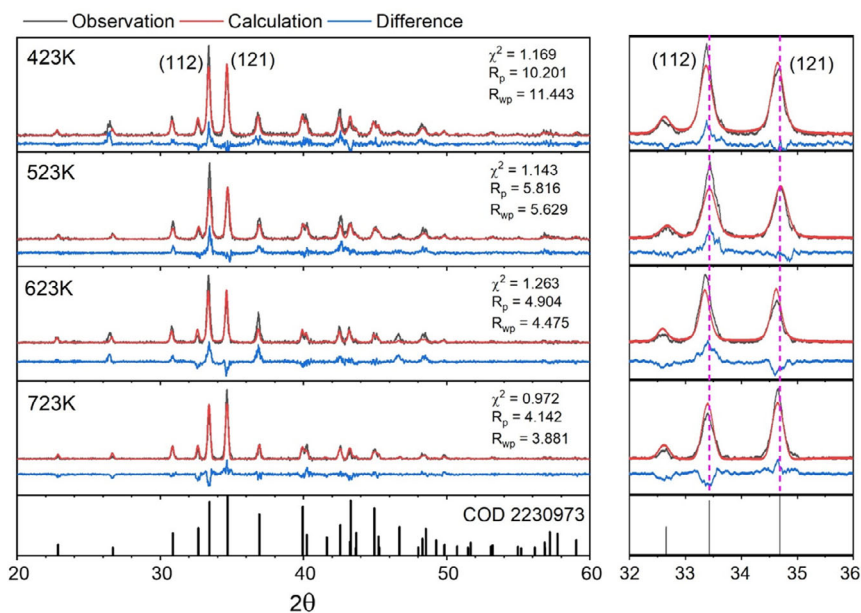

Figure 1. XRD patterns of the bulk Ag$_2$Se samples sintered at different SPS temperatures. The right-hand images show the expanded view for the two main peaks at the (112) and (121) planes.

2300082 (2 of 7)

**ADVANCED
SCIENCE NEWS**

www.advancedsciencenews.com

**ADVANCED
ENERGY & SUSTAINABILITY
RESEARCH**
Open Access

www.advenergysustres.com

Table 1. The lattice parameters, unit cell volume, and crystallite size, calculated from X-ray diffraction patterns, the density measured from the dimensions of pellet samples, and the pore size measured from SEM images, for the bulk Ag_2Se samples sintered at different SPS temperatures.

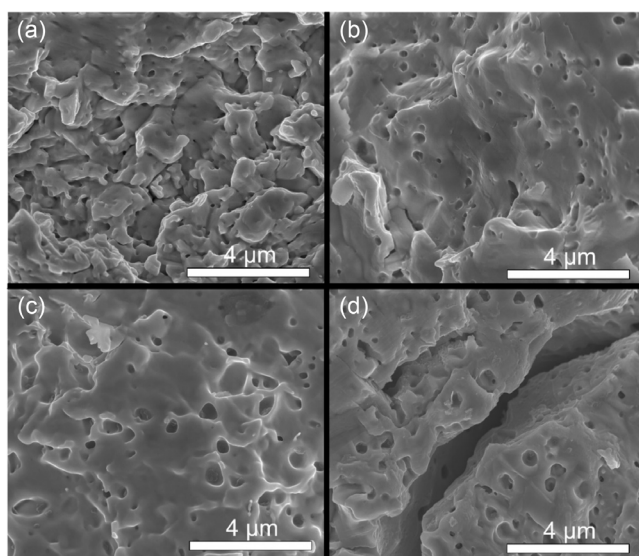| Sintering temperature	Lattice parameter [Å]				Crystallite size [nm]	Density		Pore size [nm]
	a	b	c	Volume		[g cm^{-3}]	[%]	
423 K	4.335	7.072	7.788	238.8	287 ± 8	7.823	95.21	202 ± 36
523 K	4.343	7.074	7.786	239.2	314 ± 20	7.775	94.64	372 ± 88
623 K	4.336	7.059	7.769	237.8	358 ± 15	7.812	95.08	455 ± 126
723 K	4.349	7.075	7.773	239.2	367 ± 8	7.326	89.17	503 ± 98
Ref: COD 2230973	4.336	7.070	7.774	238.3	–	–	–	–

Figure 2. SEM images from the fractured surface of the bulk Ag_2Se samples sintered at different SPS temperatures: a) 423 K, b) 523 K, c) 623 K, and d) 723 K.

The grain boundaries are still observed for the sample sintered at 423 K (Figure 2a) but seem to disappear for the sintering temperature at 523 K and above (Figure 2b–d). At high sintering temperatures, the grains seem to fuse together from the effect of SPS compaction using a high pressure (300 MPa), making it difficult to distinguish individual grains. In addition, the sample sintered at the highest temperature (723 K) contained some cracks with widths of 0.5–1 μm and lengths of 5–15 μm (Figure 2d). These cracks cause a drop in the samples' density (Table 1). The cracks are formed all over the sample, as can be seen from a low-magnification SEM image (Figure S1, Supporting Information). Furthermore, the homogeneous distribution of Ag and Se is confirmed from the energy-dispersive spectroscopy (EDS) mapping, as shown in Figure S2, Supporting Information. The EDS mapping did not show any elemental segregation. Also, the ratio between Ag and Se elements is close to the stoichiometry of Ag_2Se. The density of the samples sintered at 423–623 K is more than 94% of the theoretical value, while the sample sintered at 723 K exhibits a density of only 89%. Moreover, another interesting feature observed from the SEM images is porosity at the grain surface. These nanopores are particularly obvious for the samples

sintered at higher temperatures, possibly due to the fast fusion from SPS.[15] The pore sizes are in the range of 200–500 nm, as tabulated in Table 1.

The observed porosity and fractured structures from the sample's morphology are critically important to the TE properties of Ag_2Se since they can disturb electrical transport, possibly by suppressing activated charge carriers. To elucidate the effect of the microstructural changes on electron transport, the charge carrier concentrations were measured via the Hall measurements, as shown in **Figure 3**. The carrier concentrations in all samples increase with increasing temperatures, confirming the semiconducting behavior of Ag_2Se. Compared between the samples, it is found that the sample sintered at the lowest temperature (423 K) exhibits the largest carrier concentration, ranging from 1.5×10^{19} cm^{-3} at 300 K to 3.0×10^{19} cm^{-3} at 400 K. Raising the sintering temperatures leads to a monotonic drop in the carrier concentration. At 300 K, the carrier continuously reduces to 0.8×10^{19}, 0.7×10^{19}, and 0.5×10^{19} cm^{-3}, for the samples sintered at 523, 623, and 723 K, respectively. The decrease in the carrier concentration is attributed to the defects presented in the Ag_2Se structure. In addition to the carrier concentration, the carrier mobility was measured, as shown in Figure S3, Supporting Information. The mobility of all samples is in the range of ≈1000–1200 cm^2/Vs at 300 K, which is comparable to the reported values in literature.[15,19,23,24]
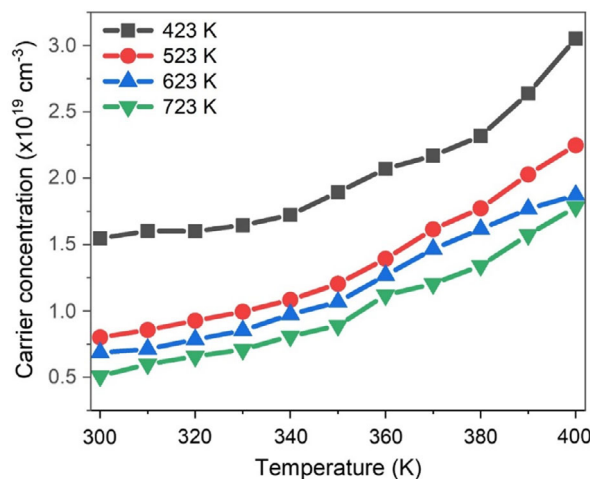

Figure 3. Temperature-dependent carrier concentrations of the bulk Ag_2Se samples sintered at different SPS temperatures.

Carrier concentration manipulation by varying sintering temperatures contributed to the decreased electrical conductivity (σ), according to Equation (2)

$$\sigma = ne\mu \tag{2}$$

where n, e, and μ are the carrier concentration, charge of an electron, and carrier mobility, respectively. As shown in **Figure 4**a, the sample sintered at 423 K exhibits the highest σ of 2.6×10^5 S m^{-1} at 310 K and increased to 3.4×10^5 S m^{-1} at 390 K, owing to its high density and the smallest microstructural porosity. Alternatively, the 723 K sample possessed the lowest σ of 1.0×10^5 S m^{-1} at 310 K and 1.5×10^5 S m^{-1} at 393 K. Decreased electrical conductivity is possibly caused by the presence of nanopores and cracks in the Ag$_2$Se structure. Moreover, the measured σ for all SPS conditions tends to increase with temperature, indicating a narrow band gap semiconducting behavior of Ag$_2$Se. The activation energy (E_a) for electron conduction can be evaluated by plotting ln(σ) versus $1/T$, according to Equation (3), assuming that the carrier mobility varies as $T^{-3/2}$[25,26]

$$\ln(\sigma) = -\frac{E_a}{2k_B}\frac{1}{T} + A \tag{3}$$

where k_B and A are Boltzmann's constant and a fitting constant. The results are shown in Figure 4b and the outcome E_a are 0.07,

0.14, 0.16, and 0.19 eV for the samples sintered at 423, 523, 623, and 723 K, respectively. The increased E_a with increasing SPS temperatures could be interpreted as the electron transport is disrupted as more pores and fractures are presented in the Ag$_2$Se structures.

Figure 4c shows the temperature-dependent plot of the Seebeck coefficient (S). The negative S values indicate the n-type semiconductor behavior of Ag$_2$Se. Moreover, the magnitude of S tends to decrease with increasing measurement temperature, confirming the narrow bandgap semiconducting behavior. The SPS temperature has a direct impact on the S values of each sample. The sample sintered at 423 K exhibits a relatively low S of -100 µV K^{-1} at 310 K and -85 µV K^{-1} at 393 K. The absolute S tends to increase at higher sintering temperatures. The sample sintered at 723 K exhibits the highest S magnitude of -150 µV K^{-1} at 310 K and -115 µV K^{-1} at 393 K. The reason for the significant increase in S magnitude with sintering temperature could be due to the decreased carrier concentration (n), according to Equation (4)[6]

$$S = \frac{8\pi^2 k_B^2}{3eh^2} m^* T \left(\frac{\pi}{3n}\right)^{\frac{2}{3}} \tag{4}$$

where h and m^* are Plank's constant and effective mass, respectively. Equation (4) explicitly tells us that the decrease in the absolute S is caused by a reduced carrier concentration. Thus, increasing SPS temperatures resulted in the depleted active
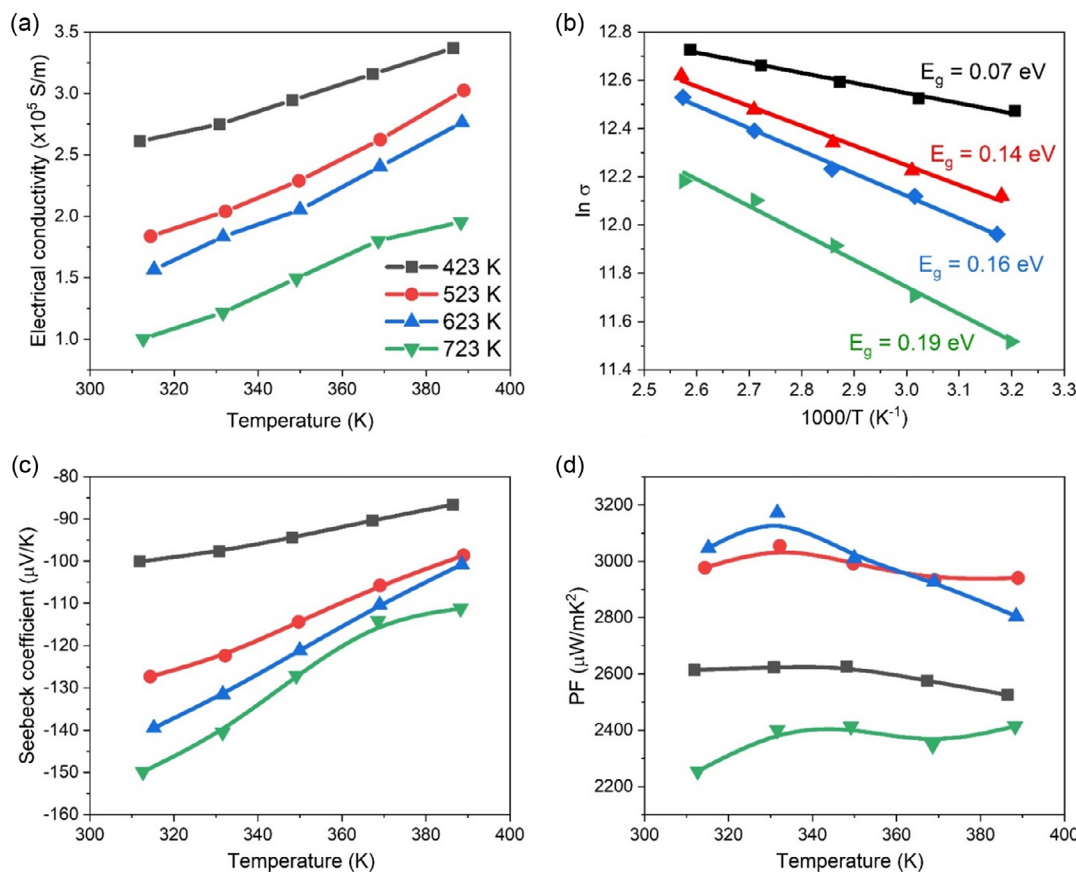

Figure 4. Temperature-dependent a) electrical conductivity, b) natural log of electrical conductivity, c) Seebeck coefficient, and d) power factor, of the bulk Ag$_2$Se samples sintered at different SPS temperatures.

**ADVANCED
SCIENCE NEWS**

www.advancedsciencenews.com

**ADVANCED
ENERGY & SUSTAINABILITY
RESEARCH**
Open Access

www.advenergysustres.com

charge carrier. This interpretation agrees well with our previous discussion on σ, which decreased with increasing SPS temperatures from lowering carrier concentration.

Figure 4d presents the plot of the power factor ($S^2\sigma$) against measurement temperature. The power factors of all samples are above 2200 μW m^{-1} K^{-2} throughout the measurement temperature range. These values are comparable to those reported in the literature for doped Ag$_2$Se or nanostructured bulk Ag$_2$Se fabricated with moderate pressure.[14,15,19,27,28] The SPS temperature shows an influential effect on the power factor. The highest power factor above 3000 μW m^{-1} K^{-2} at around 330 K was observed for the samples sintered at moderate temperatures (523–623 K). The samples at low (423 K) and high (723 K) SPS temperatures exhibit poorer power factors of 2600 and 2250 μW m^{-1} K^{-2} at room temperature, respectively.

The thermal conductivity measurement of the samples, presented in **Figure 5**a, tends to increase with measurement temperatures. This is understandable since thermal conductivity (κ) consists of lattice thermal conductivity (κ_l) and electronic thermal conductivity (κ_e). The κ_e is related to σ according to the Wiedemann–Franz law

$$\kappa_e = \sigma L T \tag{5}$$

where L is Lorentz number (1.8×10^8 WΩ K^{-2} for Ag$_2$Se).[29] Since the σ of all samples increase with temperature (Figure 4a), it is reasonable that the κ graphs vary linearly with temperature. Compared between samples, it is seen that the sample sintered at the lowest SPS temperature (423 K) shows the highest κ of 1.5 W mK^{-1} at 300 K and 2.2 W mK^{-1} at 390 K. Increasing SPS temperature results in the decreased κ throughout the temperature range. The sample sintered at 723 K exhibits the lowest κ of 0.79 W mK^{-1} at 300 K and 1.10 W mK^{-1} at 393 K. The decrease in κ for the samples with high SPS temperatures is likely to be from the defects in the samples. As mentioned earlier, nanopores and fractures were presented in the high-temperature SPS samples; these defects can scatter phonon effectively, thus suppressing κ_l. Thus, the overall thermal conductivity is reduced with higher SPS temperatures.

Figure 5b shows the temperature-dependent ZT plots. Although the samples sintered at 523–623 K showed the highest power factor, their relatively higher κ values do not foster the ZT. The maximum ZT values for these groups are about 0.78–0.83. In contrast, the sample sintered at 723 K exhibits the lowest power factor. However, due to its lowest κ, it shows the highest ZT compared to the other samples throughout the measurement temperature range. The maximum ZT of 0.90 was recorded at near room temperature (333 K). Interestingly, the ZT values of this sample are quite stable from room temperature to 400 K, with a deviation of only 0.05. It can be interpreted that our samples can operate over wide temperature ranges while the efficiency decreases only slightly. In the published literature, pristine Ag$_2$Se exhibited ZT at room temperature of about 0.5–0.8,[15,23] whereas the ZT of doped and composited Ag$_2$Se was in the range of 0.8–0.9 at room temperature.[19,30] **Figure 6** shows a comparative chart of the ZT published in the literature and the measured ZT of Ag$_2$Se at room temperature in this work. It is clearly demonstrated that our research presents a very high ZT value among the published data. It implies that the current method (SPS with high compression) could be the key to achieve the bulk Ag$_2$Se with high TE performance. Further development of this route on doped or
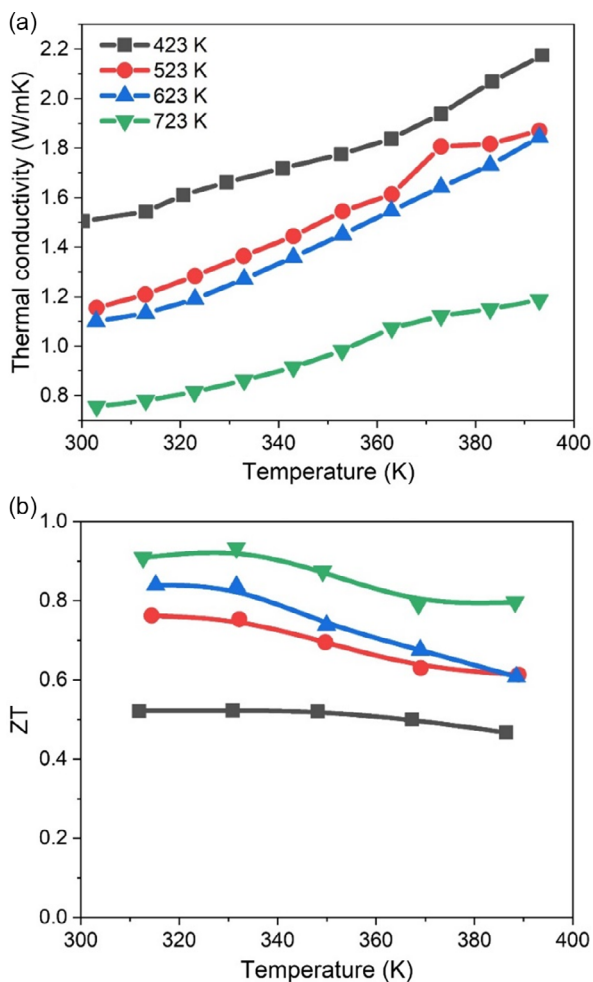

Figure 5. Temperature-dependent a) thermal conductivity and b) ZT of the bulk Ag$_2$Se samples sintered at different SPS temperatures.
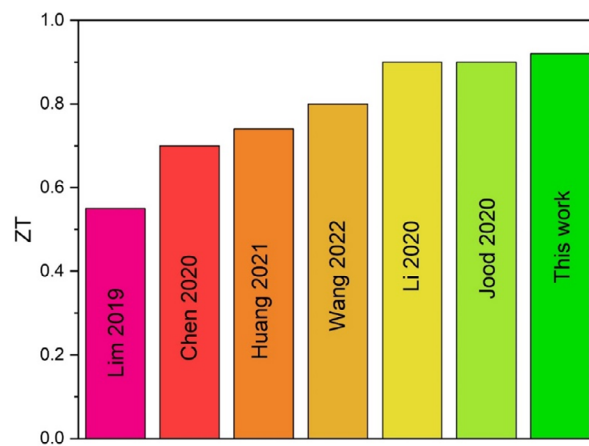

Figure 6. Comparison between the experimental ZT values at room temperature from various sources and the measured ZT in the current study.

composited Ag_2Se could promote the *ZT* and TE efficiency even more.

3. Conclusion

This research fabricated bulk Ag_2Se samples via the SPS process from Ag_2Se powders synthesized from a wet-chemical method. The SPS compression was done in a hardened steel die with a high pressure of 300 MPa. The sintering temperature was varied from 423 to 723 K. It was found that all samples showed the same orthorhombic β-Ag_2Se phase with invariant lattice parameters, but the crystallite sizes increased with increasing SPS temperatures. Moreover, as the sintering temperature was higher, the grain boundaries disappeared since the neighboring grains seemed to fuse together. Nanopores and some cracks were observed on the grain surfaces, especially in the samples sintered at higher temperatures, which significantly affect the TE properties. The electrical conductivity decreases, but the Seebeck coefficient increases with increasing sintering temperatures. These observations were attributed to the presence of defects in the structure, which reduced charge carrier concentration. The thermal conductivity also decreases with increasing SPS temperatures from enhanced phonon scattering due to microstructural defects. As a result, the *ZT* of the sample sintered at 723 K exhibited the highest value of 0.90 at 333 K, even though it possesses the smallest power factor in this sample group. The observed *ZT* was larger than many previous reports on bulk Ag_2Se. Moreover, the *ZT* of the present work was relatively stable from room temperature to 400 K, making the Ag_2Se fabricated via this route practically useful, particularly for TE generators at this temperature range.

4. Experimental Section

Materials: Silver nitrate ($AgNO_3$, 99.8%) was purchased from ACL Labscan. Selenium powder–100 mesh (Se, 99.5%) was obtained from Sigma-Aldrich. Sodium sulfite (Na_2SO_3, 98%) was purchased from Quality Regent Chemical. All chemicals were used as received with no further purification.

Preparation of Ag_2Se Powder: First, 1.5125 g of Na_2SO_3 was dissolved in 120 mL of deionized (DI) water at 373 K. Then, 0.9478 g of Se powder was added under magnetic stirring for 30 min. A clear solution of sodium selenosulfate (Na_2SeSO_3) was obtained according to the chemical reaction: $Na_2SO_3 + Se \rightarrow Na_2SeSO_3$.

A second solution of 4.0772 g of $AgNO_3$ in 240 mL DI water was prepared and poured into the first solution after it was cooled to room temperature. The mixed solution was stirred continuously for 2 h to complete the reaction. After that, Ag_2Se precipitates were collected and rinsed with DI water several times, followed by several rinses in ethanol. Finally, the powder was dried in an oven at 353 K overnight.

Preparation of Bulk Ag_2Se: A 3 g mass of Ag_2Se powder was used for each compaction in SPS. A super-hard die with a diameter of 12.7 mm was used. Then, the powder was loaded into a hardened steel die, covered with a molybdenum (Mo) sheet, and sintered at 423, 523, 623, and 723 K with a heating rate of 50 K min^{-1}. Samples were held at the final temperature for 10 min under a pressure of 300 MPa and an argon (Ar) atmosphere.

Characterization: Bulk samples were hand crushed in a mortar to prepare them for X-ray diffraction (XRD, Ultima IV, Rigaku) analysis to identify phases and crystallinity. A scanning electron microscope (SEM, JSM-6500F, JEOL) was used to observe the microstructure at the fractured surface. Hall measurement was used to measure the carrier concentration (*n*) from 300 to 400 K under a high-vacuum atmosphere with variable magnetic fields from −1.0 to 1.0 T (Versalab, Quantum Design). The thermal conductivity (*κ*) of the polished bulk sample was observed using laser flash analysis from room temperature to 400 K under an Ar atmosphere (LFA-457, Netzsch). Then, the samples were cut into rectangular pieces. The four-point probe principle was used to measure the electrical conductivity (*σ*) and Seebeck coefficient (*S*) from room temperature to 400 K under a helium (He) atmosphere (ZEM-3, ULVAC).

Conflict of Interest

The authors declare no conflict of interest.

Data Availability Statement

The data that support the findings of this study are available from the corresponding author upon reasonable request.

[1] R. M. Ambrosi, H. Williams, E. J. Watkinson, A. Barco, R. Mesalam, T. Crawford, C. Bicknell, P. Samara-Ratna, D. Vernon, N. Bannister, D. Ross, J. Sykes, M.-C. Perkinson, C. Burgess, C. Stroud, S. Gibson, A. Godfrey, R. G. Slater, M. J. Reece, K. Chen, K. Simpson, R. Tuley, M. Sarsfield, T. P. Tinsley, K. Stephenson, D. Freis, J.-F. Vigier, R. J. M. Konings, C. , M. Libessart, et al. *Space Sci. Rev.* **2019**, *215*, 55.

[2] C. Barklay, D. Kramer, C. Whiting, R. Ambrosi, R. Mesalam, in *presented at IEEE Aerospace*, Big Sky, MT, 7–14 March **2020**, 4667.

[3] C. Candolfi, S. E. Oualid, D. Ibrahim, S. Misra, O. E. Hamouli, A. Léon, A. Dauscher, P. Masschelein, P. Gall, P. Gougeon, C. Semprimoschnig, B. Lenoir, *CEAS Space J.* **2021**, *13*, 325.

[4] L. C. Robert, L. B. Gary, in *Radioisotopes* (Ed: S. Nirmal), IntechOpen, Rijeka **2011**, Ch. 22, https://doi.org/10.5772/23914.

[5] J. Yang, T. Caillat, *MRS Bull.* **2006**, *31*, 224.

[6] G. J. Snyder, E. S. Toberer, *Nat. Mater.* **2008**, *7*, 105.

[7] S. Wongprakarn, S. Pinitsoontorn, S.-a. Tanusilp, K. Kurosaki, *Phys. Status Solidi A* **2017**, *214*, 1700235.

[8] S. Wongprakarn, S. Pinitsoontorn, S. Tanusilp, K. Kurosaki, *Mater. Sci. Semicond. Process.* **2018**, *88*, 239.

[9] A. D. Lalonde, P. D. Moran, *J. Electron Mater.* **2010**, *39*, 8.

[10] Y. Xiao, L.-D. Zhao, *npj Quantum Mater.* **2018**, *3*, 55.

[11] Q. Zhang, F. Cao, W. Liu, K. Lukas, B. Yu, S. Chen, C. Opeil, D. Broido, G. Chen, Z. Ren, *J. Am. Chem. Soc.* **2012**, *134*, 10031.

[12] T. I. Witting, C. T. Chasapis, F. Ricci, M. Peters, A. N. Heinz, G. Hautier, J. Snyder, *Adv. Electron. Mater.* **2019**, *5*, 1800904.

[13] M. W. Ashraf, S. I. Haider, A. R. Solangi, A. F. Memon, *Phys. Sci. Rev.* **2022**, https://doi.org/10.1515/psr-2021-0112.

[14] F. F. Aliev, B. M. Jafarov, I. V. Eminova, *Semiconductor* **2009**, *43*, 977.

[15] J. Chen, Q. Sun, D. Bao, T. Liu, W. D. Lui, C. Liu, J. Tang, D. Zhou, L. Yang, Z. G. Chen, *ACS Appl. Mater. Interfaces* **2020**, *12*, 51523.

[16] D. Li, J. H. Zhang, J. M. Li, J. Zhang, X. Y. Qin, *Mater. Chem. Front.* **2020**, *4*, 875.

[17] Y. Ding, Y. Qiu, K. Cai, Q. Yao, S. Chen, L. Chen, J. He, *Nat. Commun.* **2019**, *10*, 841.

[18] M. Ferhat, J. Nagao, *J. Appl. Phys.* **2000**, *88*, 813.

[19] P. Jood, R. Chetty, M. Ohta, *J. Mater. Chem. A* **2020**, *8*, 13024.

[20] P. Jood, M. Ohta, *ACS Appl. Energy Mater.* **2020**, *3*, 2160.

[21] N. Jakhar, D. K. Kedia, A. Kumar, K. Saurabh, S. Singh, *Appl. Phys. Lett.* **2023**, *122*, article no. 163901.

[22] A. L. Patterson, *Phys. Rev.* **1939**, *56*, 978.

[23] S. Huang, T.-R. Wei, H. Chen, J. Xiao, M. Zhu, K. Zhao, X. Shi, *ACS Appl. Mater. Interfaces* **2021**, *13*, 60192.

[24] M. Jin, J. Liang, P. Qiu, H. Huang, Z. Yue, L. Zhou, R. Li, L. Chen, X. Shi, *J. Phys. Chem. Lett.* **2021**, *12*, 8246.

[25] R. Dalven, R. Gill, *Phys. Rev.* **1967**, *159*, 645.

[26] H. Wang, W. Chu, D. Wang, W. Mao, W. Pan, Y.-J. Guo, Y. Xiong, H. Jin, *J. Electron. Mater.* **2011**, *40*, 624.

[27] J. Liang, P. Qiu, Y. Zhu, H. Huang, Z. Gao, Z. Zhang, X. Shi, L. Chen, *Research* **2020**, *2020*, 6591981.

[28] K. H. Lim, K. W. Wong, Y. Liu, Y. Zhang, D. Cadavid, A. Cabot, K. M. Ng, *J. Mater. Chem. C* **2019**, *7*, 2646.

[29] C. Jiang, Y. Ding, K. Cai, L. Tong, Y. Lu, W. Zhao, P. Wei, *ACS Appl. Mater. Interfaces* **2020**, *12*, 9646.

[30] H. Wang, X. Liu, Z. Zhou, H. Wu, Y. Chen, B. Zhang, G. Wang, X. Zhou, G. Han, *Acta Mater.* **2022**, *223*, 117502.